Performance Assessment of the Optical Transient Detector and Lightning Imaging Sensor. Part I: Predicted Diurnal Variability

DENNIS J. BOCCIPPIO, WILLIAM J. KOSHAK, AND RICHARD J. BLAKESLEE

NASA Marshall Space Flight Center, Huntsville, Alabama

(Manuscript received 27 August 2001, in final form 11 January 2002)

ABSTRACT

Laboratory calibration and observed background radiance data are used to determine the effective sensitivities of the Optical Transient Detector (OTD) and Lightning Imaging Sensor (LIS), as functions of local hour and pixel location within the instrument arrays. The effective LIS thresholds, expressed as radiances emitted normal to cloud top, are 4.0 ± 0.7 and 7.6 ± 3.3 μJ sr^{-1} m^{-2} for night and local noon; the OTD thresholds are 11.7 ± 2.2 and 16.8 ± 4.6 μJ sr^{-1} m^{-2}. LIS and OTD minimum signal-to-noise ratios occur from 0800 to 1600 local time, and attain values of 10 ± 2 and 20 ± 3, respectively. False alarm rate due to instrument noise yields ~5 false triggers per month for LIS, and is negligible for OTD. Flash detection efficiency, based on prior optical pulse sensor measurements, is predicted to be 93 ± 4% and 73 ± 11% for LIS night and noon; 56 ± 7% and 44 ± 9% for OTD night and noon, corresponding to a 12%–20% diurnal variability and LIS:OTD ratio of 1.7. Use of the weighted daily mean detection efficiency (i.e., not controlling for local hour) corresponds to σ = 8%–9% uncertainty. These are likely overestimates of actual flash detection efficiency due to differences in pixel ground field of view across the instrument arrays that are not accounted for in the validation optical pulse sensor data.

1. Introduction

The Lightning Imaging Sensor (LIS; 1997–present) and Optical Transient Detector (OTD; 1995–2000) are low earth orbit (LEO) instruments that detect optical pulses from lightning flashes, during both day and night. Instrument design and deployment has been described in Christian et al. (1992, 1996, 1999), and laboratory calibration results have been reported by Koshak et al. (2000a). Statistical ground validation of the OTD by the ground-based National Lightning Detection Network was reported by Boccippio et al. (2000b), while ground validation of the LIS using small-sample case studies of very high frequency (VHF) time-of-arrival network data has been reported by Ushio et al. (1999), Thomas et al. (2000), and Koshak et al. (2000b). The nominal LIS design specifications (Christian et al. 1992) were to achieve a 4.7 μJ sr^{-1} m^{-2} operating threshold, yielding a 90% flash detection efficiency [based on studies by Christian and Goodman (1987), discussed below], although the variability of this threshold with time-of-day and across the field of view (FOV) were not specified.

The focus of this series of papers is a performance assessment of the OTD and LIS, with emphasis on yielding results applicable for research use and instructive for new instrument design. A complete performance assessment addresses the instruments' accuracy, response, bias, and variance. This study deals with instrument sensitivity and thresholds, the simplest metrics of instrument response. LIS and OTD nighttime sensitivity for near-boresight pixels, as determined by laboratory calibration, has been reported by Koshak et al. (2000a). LIS and OTD pixel sensitivity is expected to vary across the instrument field of view and with background intensity, hence assessing the operational performance of these instruments requires physical understanding of off-boresight instrument response, extension of the laboratory data to daytime conditions, and information about daytime background intensity. When combined with independent or bootstrapped estimates of pulse radiance distributions in lightning strokes or flashes, the instrument detection efficiency for these features may be modeled. This study utilizes independent measurements of pulse radiance distributions. Future papers in the series will deal with bootstrapped pulse radiance distributions, LIS and OTD sampling-related variance, ground validation, and performance of optical pulse-to-flash and flash-to-cell clustering algorithms.

Modeling and prediction of the sensitivity and detection efficiency, as distinct from cross-sensor validation, are desirable goals. The consistency of modeled results may be verified by ground validation, and in

Corresponding author address: Dennis J. Boccippio, National Space Science and Technology Center, NASA Marshall Space Flight Center SD-60, Huntsville, AL 35812.
E-mail: Dennis.Boccippio@msfc.nasa.gov

some cases, inconclusive validation results from small-sample case studies may be placed in context by the predicted response. More importantly, a self-consistent and verified working model of instrument response is critical for the design and deployment of similar or improved optical detectors. Such a model is particularly important for geostationary earth orbit (GEO) deployment (Christian et al. 1989), where a near-stationary instrument field of view implies that response nonuniformties across the FOV will covary with actual geophysical variability. In LEO, such nonuniformity simply increases the variance of observations; in GEO, it introduces a bias, unless corrected through calibration of the observed data. Other applications of this study include estimating intrinsic measurement variance (i.e., assigning error bars in nonsampling-limited cases) and creation of controlled pulse radiance distribution datasets for correlative or predictive purposes (i.e., identifying a maximum operating thresold radiance, and filtering all pixel observations that fall below this radiance). Examples of the latter could include investigations into correlating pulse radiance with independently measured flash electrical energetics, or categorization of flashes as intracloud or cloud to ground based on their observed optical properties.

The general procedure to be followed in this study is as follows:

1) Estimate the minimum detectable radiance I_0 of each instrument pixel (x, y) as a function of local time of day τ.
2) Estimate the flash detection efficiency (i.e., the detectable percentage of true flashes, defined as contiguous channel structures) of each pixel using this $I_0(x, y, \tau)$.

Task 1) requires knowledge of the sensor response across the FOV [reported by Koshak et al. (2000a) for near-boresight angles, and generalized here], as well as the actual statistical distribution of background intensity (reported here). While an analysis in terms of solar zenith angle would be most physically appropriate, the local hour analysis is believed to adequately capture the salient characteristics of instrument sensitivity. Task 2) requires a ''truth'' mapping of flashes detectable for a specified I_0. Koshak et al. (2000a) utilized a 257-flash sample of optical pulse sensor measurements at night (Christian and Goodman 1987; Goodman et al. 1988) in the southeast United States; we use the same mapping in this study. Comparable statistical samples are rare, although an alternative approach, used in the second paper in this series, is to use the LIS nighttime observations themselves to perform a bootstrap mapping. It is important during analysis to keep tasks 1) and 2) separable, and to pose both in a form independent of specific instrument configuration or deployment geometry, as new truth mappings may one day be available from field studies using different instruments.

2. Instrument description

Discussion of LIS and OTD performance modeling requires a brief summary of the sensor designs and operation. Detailed technical descriptions can be found in (Christian et al. 1989, 1992, 1996, 1999). The treatment below summarizes instrument operation in simple terms, to help in understanding and verifying the methodology used in this study.

a. General behavior and thresholding

Both OTD and LIS include a lens assembly, a narrowband interference filter centered on a lightning emission peak wavelength, and a charged couple device (CCD) pixellated imager. Incident radiance I passes through (and is reduced by) the aperture, lens, and filter assembly and is focused upon the pixel array. Each pixel maps a solid angle $\Delta\omega$, which varies across the FOV. Pixels accumulate energy, integrating over frames of approximately 1.9 ms. When the frame-to-frame difference in accumulated energy exceeds a prescribed energy threshold, a transient pixel ''event'' is recorded. The optical energy E collected by a pixel is converted to an analog instrument count C, either 12-bit C for the background radiance, or 7-bit c for the transient differences. There are $j = 1, \ldots, 4$ quadrants in the camera pixel array and each quadrant has its own linear gain amplifier. Hence, we denote the associated DC (background) gain[1] of each quadrant by G_j. One amplifier provides the AC (lightning) gain that we denote by g. Furthermore, $C = C(E_B(\mathbf{x}), G_j) = C(\mathbf{x}) \sim G_j E_B(\mathbf{x}) + k_j$, where the B subscript indicates ''background,'' k_j is the quadrant offset, and $G = G(\mathbf{x}) = G_j$ is understood. The AC (lightning) count is more complicated and can be written as $c = c(E_L, E_B, g)$, where the L subscript indicates ''lightning.''[2] It is important to note that thresholds are prescribed as counts (energies), not radiances, hence the transformation of emitted radiance to observed radiance, and observed radiance to pixel energy and analog counts, is important, as this transformation varies across the instrument FOV. The natural distributions that are key inputs to determining the instrument detection efficiency are best described by their emitted radiance, but the observations are fundamentally of pixel energy.

A further complication of instrument operation is that the transient threshold varies automatically (via a lookup table) with background radiance, to guard against instrument noise during bright background scenes. This threshold is not routinely recorded for every pixel and every frame, hence it must be statistically estimated from the population of background radiances of light-

[1] In this discussion, ''DC'' refers to measurements or calibration of the background radiance, while ''AC'' refers to the transient optical pulse response.

[2] The AC amplifier is logarithmic for OTD, piecewise linear for LIS.

ning-capable clouds. The dependence of c on E_B is a further implicit effect.

The complete transformation of radiance I incident upon the lens at a pixel $\mathbf{x} = (x, y)$ with off-boresight angle $\theta(\mathbf{x})$ and CCD-relative azimuth $\phi(\mathbf{x})$, to the pixel energy E, is given by

$$E(\mathbf{x}) = q(\mathbf{x}) \int_{\Delta t} \int_{\Delta\omega} \int_{\Delta\lambda} I_\lambda(\omega, t) L_\lambda(\theta, \phi)\, d\lambda\, d\omega\, dt. \tag{1}$$

Here, I_λ has units of W m^{-2} sr^{-1} μm^{-1}. The m^{-2} units relate to the entrance aperture a, not the pixel ground footprint. In all subsequent discussion, I will be expressed in units of μJ m^{-2} sr^{-1}, the integration over frame time Δt and filter bandwidth $\Delta\lambda$ being implicit. The $q(\mathbf{x})$ is the pixel quantum efficiency, and will be assumed constant. Here $L_\lambda(\theta, \phi)$ represents the net reduction of incident I_λ by passage through the aperture/lens/filter assembly at off-boresight aperture/lens incidence and nonnormal incidence upon the CCD array, and has units of m^2; these units reflect the component of L_λ relating to the effective aperture $a(\theta)$.

For a DC (stationary) radiance, the energy is thus,

$$E(\theta, \phi) = IqL(\theta, \phi)\Delta\omega(\theta, \phi), \tag{2}$$

where we have integrated over bandwidth $\Delta\lambda$ and the (θ, ϕ)-dependent terms can be lumped into a general response function $R(\theta)$, reflecting azimuthal symmetry and all effects prior to the instrument amplifiers, hence,

$$E(\theta) = IR(\theta). \tag{3}$$

Here R applies to both stationary and transient observed broadband radiances. Its relative dependence on θ may be determined from the laboratory DC background calibrations. Since the DC gain is nearly linear, the ratio of observed counts within the jth quadrant at θ_0 (boresight) and θ_1 (off boresight) for a fixed incident I directly yields R:

$$R'(\theta_1) = \frac{R(\theta_1)}{R(\theta_0)} = \frac{C(I_B, \theta_1) - k_j}{C(I_B, \theta_0) - k_j}. \tag{4}$$

Further, the noise floor k_j is small and can be neglected if I_B is large. Figure 1 shows $R'(\theta)$ for LIS and OTD. The inferred $R'(\theta)$ is found to be independent of the magnitude of the background radiance I_B, and contains ~2% scatter from nonuniformity of the DC calibration source (not shown). For θ corresponding to the array corners ($\theta_{\max} \sim 49°$ for both OTD and LIS), approximately 82%–84% of the incident I passed at boresight will be passed at $\theta_{\max}$.

At night, with no appreciable background radiance, a fixed-count instrument threshold c_0 is effectively a fixed-energy threshold. If this fixed-energy threshold is applied at boresight $E(\mathbf{x}_0)$ and off-boresight $E(\mathbf{x}_1)$, the minimum detectable radiances I_0 within a quadrant may thus be related:

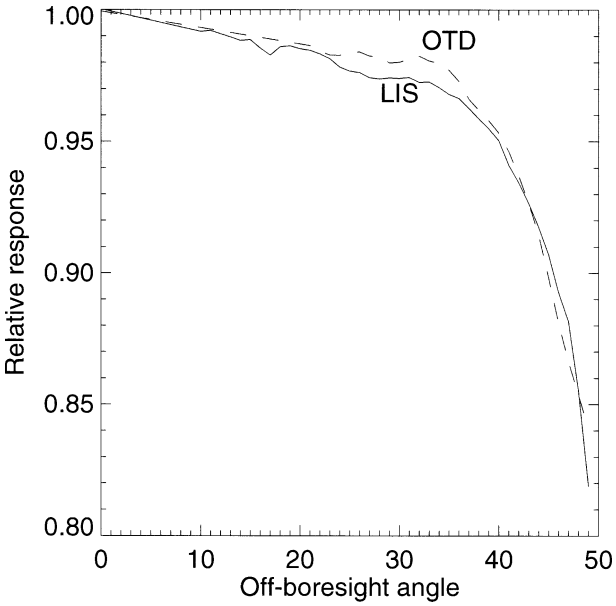

FIG. 1. Response function $R'(\theta)$ for the OTD and LIS sensors, calculated from observed sensor counts under five background illumination levels, following Eq. (4).

$$\frac{I_0(\mathbf{x}_1)}{I_0(\mathbf{x}_0)} = \frac{1}{R'(\theta_1)}. \tag{5}$$

Similarly, against an identical incident nonzero background radiance I_B, the ratio of off-boresight to boresight minimum detectable radiances would be

$$\frac{I_0(\mathbf{x}_1)}{I_0(\mathbf{x}_0)} = \frac{c^{-1}(c_0, I_B R(\theta_1))}{c^{-1}(c_0, I_B R(\theta_0))} \frac{1}{R'(\theta_1)} \tag{6}$$

(no longer restricted to the same quadrant, as the gains are explicitly included).

It is clear from Eq. (5) and Fig. 1 that against the same background I_B, minimum detectable radiances (for a given energy threshold) will be higher for off-boresight pixels, regardless of their ground FOV or the relative amount of source light emitted toward the sensor. Between quadrants, variability in the DC response is important in establishing the AC minimum detectable radiance. Again, these gains have been well established as part of the laboratory calibration. Operationally, the data collected and reported by Koshak et al. (2000a) have been interpolated into complete lookup tables for $I_B = I_B(\mathbf{x}, C)$ and $I_L = I_L(j, I_B, c)$.[3] Since the AC lookup tables have been derived from laboratory tests of a small subset of sensor pixels at low observed θ^* ($\overline{\theta}^* \sim 22°$; $\overline{R}^* \sim 0.985$ for both OTD and LIS) and are operationally applied uniformly within quadrants, reported event radiances for recalibrated OTD data or distributed LIS

[3] These calibration arrays are distributed with the OTD and LIS software package; interested users should contact the authors for details on use of these data.

v4 data (e.g., Boccippio et al. (2000a) are slightly in error and should be corrected by $\overline{R}^*/R'(\theta)$.

b. Geometry during calibration and deployment

The instrument response, as described above, is now placed in the context of laboratory and orbital observational geometry. Figures 2a–c shows the sensor lens and pixel array observing a laboratory calibration source, reflected solar light, and an emitted lightning pulse. An understanding of these geometries is needed to apply laboratory calibration data, and observations from independent truthing sensors, to models of OTD and LIS performance.

In the laboratory (Fig. 2a), the instrument was canted relative to a fixed wideband emitter. Thus the radiance incident upon the lens, I_{cal}, is at full intensity and the observed pixel energy (counts) yields either the DC or AC calibration curves, depending on the nature of the test.[4]

When observing reflected solar light (Fig. 2b), the emitted radiance I_{sun} is scattered from cloud top through an unspecified function S of the local solar zenith angle ζ (itself strongly correlated to local hour τ) and the cloud-sensor angle α; together, these compose the ''glint angle'' γ. The radiance I_B incident upon the sensor is thus $I_{\text{sun}}S(\alpha + \zeta)$, and the pixel energy $E_B = E_B(\theta, \alpha + \zeta)$. This energy, expressed in counts C is passed through a lookup table to yield the prescribed transient (lightning) threshold c_0. The threshold count may then be converted, through the calibration curves and $R'(\theta)$ correction, to a minimum detectable radiance I_0 for use in detection efficiency modeling.

When observing a lightning pulse emitted from within a cloud (Fig. 2c), we must consider the differences between radiance emitted normal to cloud top I_L and radiance emitted at the sensor–cloud angle α. This latter has been written $I_L \cos\alpha$ as a crude approximation of scattering effects within the cloud [see, e.g., curves in Fig. 7 and 8 of Thomason and Krider (1982), which are pertinent if normalized to their at-boresight values]. While the precise form of the α dependence may not be a single function for all lightning–cloud geometries, it is important to realize that this effect is likely a reduction over I_L, and that this effect has not been captured in Eqs. (1), (2), or (5). However, truthing observations such as the U2 aircraft optical pulse sensor dataset are typically targeted for collection at low α, so use of these observations in modeling sensor response at high α will yield incorrect predictions. For LIS, $\alpha_{\max} \sim 53°$; for the higher-altitude OTD, $\alpha_{\max} \sim 60°$.

The general pixel trigger condition is $c_L > c_0$, that is, $E_L > E_0$ or

$$I_L \cos\alpha > I_0. \tag{7}$$

This says nothing about how individual emitters are organized within a pixel ground footprint, simply that the net radiance emitted normal to cloud top undergoes an α-dependent reduction and a θ-dependent reduction [through the $R(\theta)$ component of I_0] before it can trigger a pixel event.

For detection efficiency, modeling, and prediction a final complication must be considered. The event trigger conditions above contain implicit dependence on pixel location $\mathbf{x}$, yet observations used for truth mappings are sampled at different relative geometries. For example, the U2 optical pulse sensor (OPS) sampled one 60° pixel per lightning stroke, was flown with a goal of $\alpha \sim 0°$ geometry, and at variable altitudes a few kilometers above cloud top, yielding a range of pixel footprints.

Consider the hypothetical case (Fig. 2d) in which the U2 OPS makes an observation I^*_{OPS} of a lightning stroke that fills exactly (and no more than) its single pixel, and in which the OPS pixel footprint A_{OPS} is smaller than the footprint A_1 of an LIS off-boresight pixel $\mathbf{x}_1$. After correcting for the filter response F_{OPS}, the observation may be interpreted as an emitter distributed over A_{OPS} and observed through solid angle $\Delta\omega_{\text{OPS}}$. If the OPS pixel has $\alpha = 0°$, the same emitter, viewed by LIS pixel $\mathbf{x}_1$, would yield the equivalent net radiance $I(\mathbf{x}_1)$ toward the LIS:

$$I(\mathbf{x}_1) = \frac{I^*_{\text{OPS}} \cos\alpha_1}{F_{\text{OPS}}} \frac{A_{\text{OPS}}}{A_1}, \tag{8}$$

where the ratio of footprint areas simply reflects the smaller solid angle filled by the fixed-size source when viewed from α_1.

Similarly, an observation I^* filling an LIS boresight pixel $\mathbf{x}_0$ would yield the following radiance if it was the only emitter occuring in the pixel $\mathbf{x}_1$:

$$I(\mathbf{x}_1) = \frac{I^*(\mathbf{x}_0) \cos\alpha_1}{R(\theta_0)} \frac{A_0}{A_1}. \tag{9}$$

The expressions in Eqs. (8) and (9) transform normal cloud-top emissions from a single boresight-viewing pixel observation, of arbitrary footprint $A < A_1$, to radiance emitted toward an OTD or LIS off-boresight pixel.[5] They are thus independent of the increase in sensor minimum detectable radiance given by Eqs. (5) and (6), which relate radiances incident upon the lens.

The ratio A_1/A_0, with A_0 defined as the ground FOV of a LIS boresight pixel (12.5 km^2), is shown in Fig. 3 for LIS and OTD. LIS corner pixel FOVs are ~4 times larger than at boresight, and OTD boresight and corner pixel FOVs are 5 and 13 times larger than LIS at boresight.

The size of pixel footprints in the OPS dataset is indeterminate because precise viewing geometry was

[4] In the calibration test reported by Koshak et al. (2000a), and AC radiance was achieved by simply narrowing the duty cycle of a DC emitter. Note again that in laboratory determination of $I_L(j, I_B, c)$, the effects of $R'(\theta)$ were effectively not considered.

[5] If $A_{\text{OPS}} > A_1$, the OPS observation is LIS pixel filling, and the ratio is ''capped'' at unity.

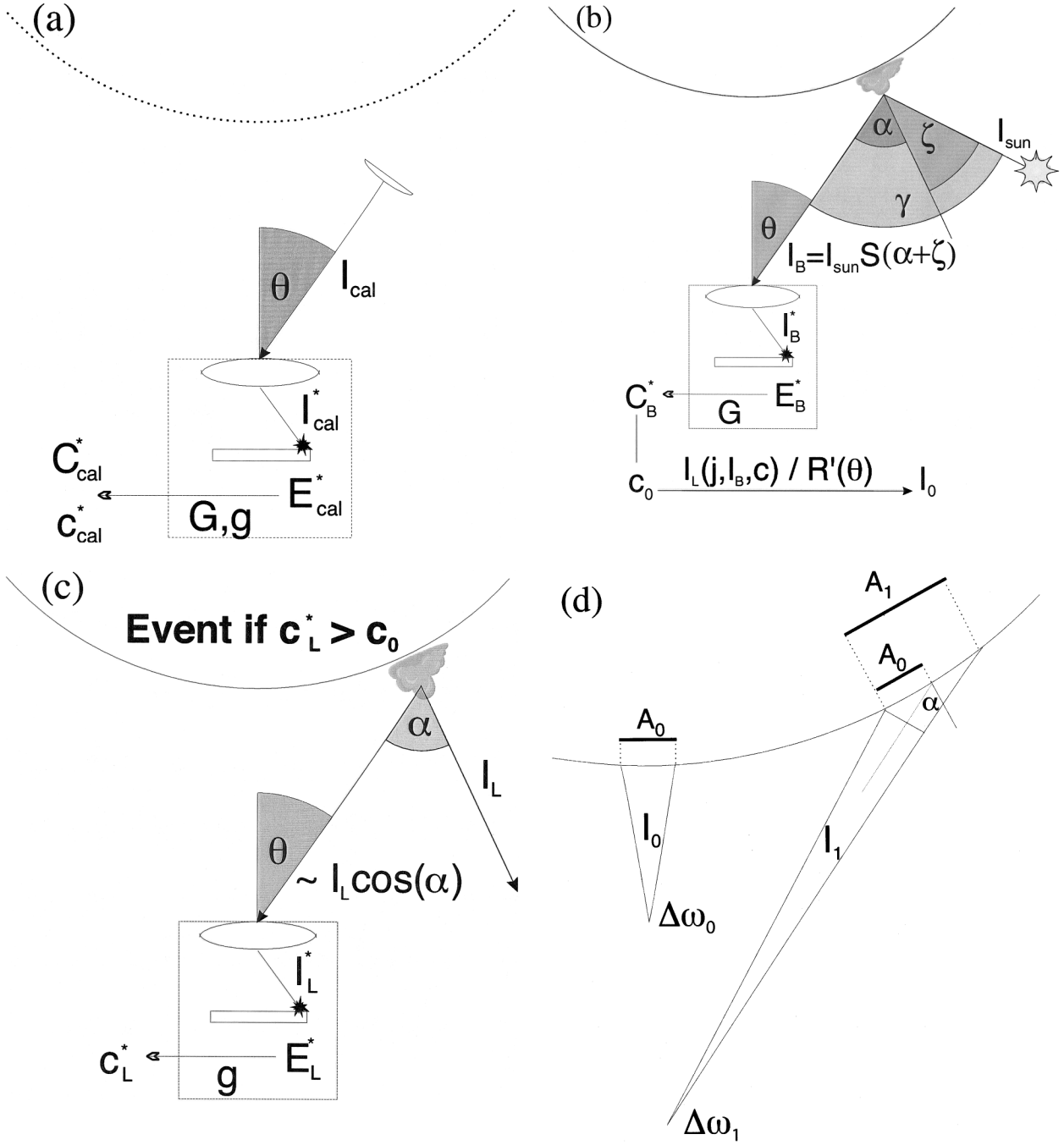

FIG. 2. (a) OTD and LIS viewing geometry for laboratory calibration sources. The aggregate results of the calibration are contained in the dashed box. (b) Viewing geometry for reflected solar light. The observed background counts C_B^* set the lightning threshold minimum detectable radiance I_0. (c) Viewing geometry for an emitted lightning pulse. We assume that on average, the radiance viewed by the sensor is less than that emitted normal to cloud top, as a result of in-cloud scattering. (d) Geometry if a given emitter J_0, over a fixed area A_0 and observed with a boresight sensor, is placed in an OTD or LIS off-boresight pixel footprint with area A_1, yielding radiance I_1 toward the sensor. Equations (7) and (8) provide the scaling.

not recorded, and the observed pixels were not necessarily completely filled by possible emitting surfaces (clouds during strokes). Use of the OPS dataset for truthing thus implicitly must assume that OPS, LIS, and OTD pixels are statistically ''comparably sized,'' an assumption with obvious drawbacks (Fig. 3). If the OPS pixel footprint was uniform, and OPS peak-event radiances per flash were used to estimate OTD or LIS flash detection efficiency [as in Koshak et al. (2000a) and section 3 of this study], then if $A_{\mathrm{OPS}} < A_1$ the results are

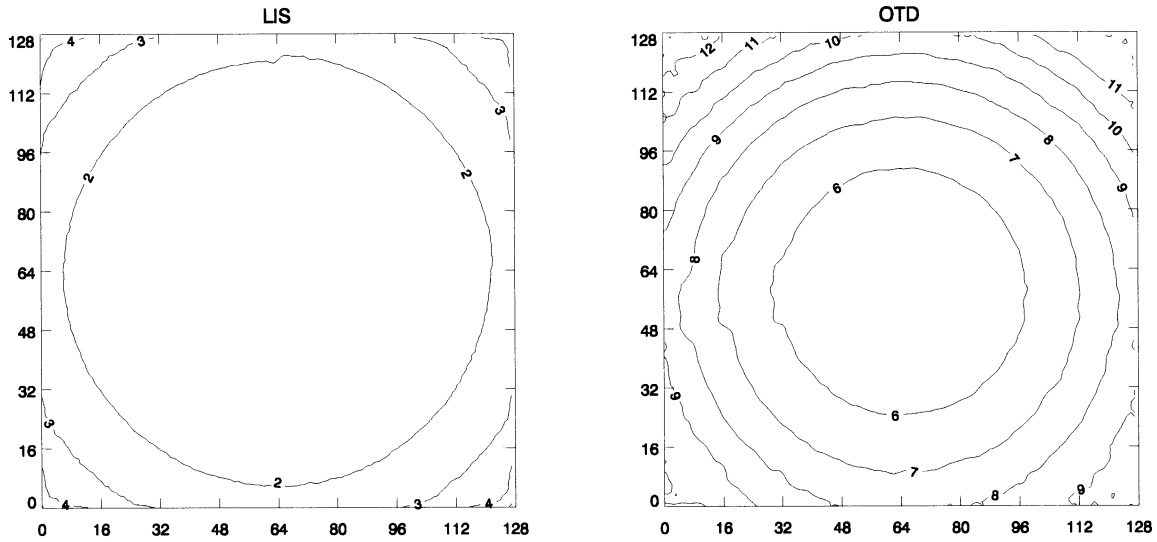

FIG. 3. Pixel footprints (mean computed FOV of all geolocated events) for (left) LIS and (right) OTD, normalized to the LIS boresight pixel footprint $A_0 = 12.5$ km^2. OTD boresight pixels are 5.1× as large as LIS boresight pixels.

inconclusive, as single-pixel OPS measurements do not provide enough information to determine off-boresight OTD and LIS observations, and flash detection efficiency predictions will be overestimates. Alternatively, if $A_{\mathrm{OPS}} > A_1$, the results are transferrable, albeit high variance (since only one OPS pixel per stroke is used to infer peak pixel radiance per flash). Given the range of likely OPS-viewing geometries, we might speculate that $\overline{A}_{\mathrm{OPS}} = A_1$ somewhere in the continuum of LIS boresight to OTD corner pixels, hence for some subset of pixels, the estimates are correct and the bulk array results are high-variance upper bounds of flash detection efficiency.

The use of LIS boresight pixel observations as a relative, bootstrapped truth mapping with controlled viewing geometry is discussed in the appendix, and will be expanded upon in the second paper in this series. In this study, we use only the U2 OPS dataset for truthing, and hence cannot explicitly account for viewing geometry effects other than cosα. It will, however, be convenient to express OTD and LIS radiance thresholds in terms of radiance emitted normal to cloud top:

$$I_0' \sim \frac{I_0}{\cos\alpha}, \tag{10}$$

thus accounting for at least one important term in Eq. (8). In this, as in all preceding expressions, the cosα term could of course be replaced by a more robust correction function of α derived, for example, from statistical modeling of various lightning–cloud geometries.

Enough information has now been presented to frame an examination of sensor response as a function of ($\mathbf{x}$, τ) (τ is local hour). To do this, we require $I_0'(\mathbf{x}, \tau)$, hence we must estimate the statistical distribution of $I_B(\alpha, \tau)$ to determine the distribution of applied energy thresholds, and thus the distribution of minimum detectable radiances.[6]

3. Diurnal variability

In this section the statistical distribution $P_{\alpha\tau}(I_B)$, the probability of observing background radiance I_B in lightning-producing clouds at local time τ and cloud-sensor angle α, is bootstrapped from LIS observations. This distribution is then used to determine applied radiance thresholds $I_0(\mathbf{x}, \tau)$ and $I_0'(\mathbf{x}, \tau)$, and hence the diurnal variability of bulk array radiance thresholds. With this information, the approach of Christian et al. (1989) is used to estimate the diurnal variability in sensor signal-to-noise ratio (SNR) and false alarm rate (FAR). Finally, $I_0'(\mathbf{x}, \tau)$ is combined with the optical pulse sensor data of Christian and Goodman (1987); Goodman et al. (1988) to predict diurnal variability in instrument flash detection efficiency.

a. Observed background radiance

As discussed in section 2b, the applied instrument thresholds are not recorded continuously as a function of ($\mathbf{x}$, t). Further, background scenes are only recorded intermittently by the LIS and OTD, as the instruments are designed to provide enough bandwidth for uninterrupted transient data, sacrificing background scene recording as needed. However, roughly 1% of all recorded

[6] Since both OTD and LIS attitudes contain negligible roll and pitch components, $\alpha = \alpha(\mathbf{x})$ for each sensor, and both variables are used below to reflect variability across the CCD pixel array. Here α, rather than $\mathbf{x}$, is the reported component of the bivariate $P_{\alpha\tau}(I_B)$ distribution in order to reflect its actual empirical determination and physically based variability.

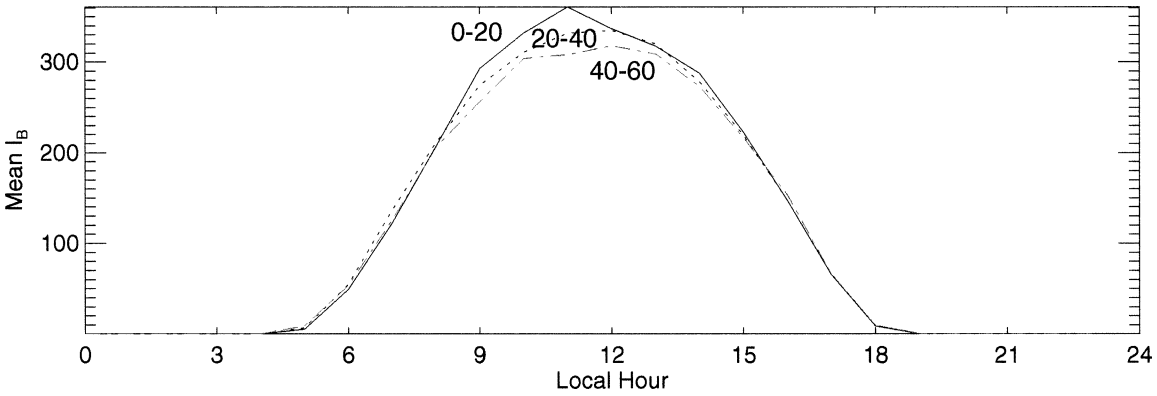

FIG. 4. Observed $\bar{I}_B$ as a function of local hour τ and cloud-sensor angle α (in α bins of 0°–20°, 20°–40°, and 40°–60°). Since the instrument response $R'(\theta)$ is included in the DC calibration, the curves reflect the mean cloud scattering effects $S(\zeta(\tau) + \alpha)$. Units are W m^{-2} sr^{-1} μm^{-1}.

pixel events are concurrent (within 1 s) with a recorded background scene. The background radiances at these pixels may thus be extracted as a sample of the population of observed radiances from lightning-capable clouds, hence estimating the desired $P_{\alpha\tau}(I_B)$. This sample will be slightly biased toward lower radiances, as events themselves are less detectable at higher background radiance, but this will be a secondary effect, as the primary use of $P_{\alpha\tau}(I_B)$ is only to estimate the applied I'_0.

Figure 4 shows the mean observed background radiances (during pixel events) as a function of (α, τ), for 20° bins of α. As expected, the dominant component is the local hour dependence of ζ, with a smaller effect due to α. Note that since α covaries with θ, incident background radiances near boresight and near local noon tend to be higher than near the array corners. In all subsequent diurnal calculations, 10° α-binned and 1-h τ-binned $P_{\alpha\tau}$ distributions are used to weight calculations, that is, for a given quantity Y and pixel location $\mathbf{x}$, partial contributions $Y(\mathbf{x}, I_B)$ are calculated for each I_B, with the mean given by

$$\overline{Y}(\mathbf{x}, \tau) = \sum_{I_B} P_{\alpha\tau}(I_B) Y(\mathbf{x}, I_B), \tag{11}$$

and the standard deviation (due to I_B variability) $\sigma_Y(\mathbf{x}, \tau)$ computed accordingly.

Similarly, footprint-weighted bulk FOV quantities $\overline{Y}(\tau)$ are computed by averaging over the pixels $\mathbf{x}$, that is,

$$\overline{\overline{Y}}(\tau) = \frac{\sum_{\mathbf{x}} \sum_{I_B} A(\mathbf{x}) P_{\alpha,\tau}(I_B) Y(\mathbf{x}, I_B)}{\sum_{\mathbf{x}} \sum_{I_B} A(\mathbf{x}) P_{\alpha\tau}(I_B)}, \tag{12}$$

and footprint-weighted standard deviations $\sigma_{\overline{Y}}(\tau)$ and $\sigma_Y(\tau)$ are calculated, representing scatter due to variability in pixel response alone, and variability in pixel response and I_B. These correspond to uncertainties appropriate for use in the likely case that a characteristic bulk array hourly value is sought, without controlling for unknown instantaneous I_B or the trajectory of a storm across the pixel array.

Finally, a weighted daily mean is computed:

$$\overline{\overline{\overline{Y}}} = \frac{\sum_{\tau} \sum_{\mathbf{x}} \sum_{I_B} A(\mathbf{x}) n_e(\tau) P_{\alpha,\tau}(I_B) Y(\mathbf{x}, I_B)}{\sum_{\tau} \sum_{\mathbf{x}} \sum_{I_B} A(\mathbf{x}) n_e(\tau) P_{\alpha\tau}(I_B)}, \tag{13}$$

along with σ_Y; here, $n_e(\tau)$ is the number of observed events at each τ in the concurrent event-background sample, and thus weights the mean for diurnal frequency of occurrence. Thus σ_Y represents the uncertainty associated with use of a single daily value, not controlling for diurnal variability.

b. Applied thresholds

Having estimated $P_{\alpha\tau}(I_B)$, the pixel minimum detectable event radiances I_0 are now estimated by the following: 1) determining the applied threshold count c_0 at each I_B, prescribed as lookup tables within the OTD and LIS instruments; 2) converting these counts to AC radiances using the calibrations $I_L(j, I_B, c)$; and 3) correcting the quadrant-uniform calibrations by $\overline{R}^*/R'(\theta)$ as described in section 2. Two sets of results are presented, one for actual radiance emitted toward the sensors I_0 and one for estimated equivalent radiances emitted normal to cloud top I'_0.

Figure 5 shows the diurnal cycle and daily mean of bulk array minimum-detectable event radiance for the OTD and LIS sensors, with $\sigma_{\overline{I}}$ and σ_I overlaid. The value of I_0 is shown by the solid curves (leftmost bars in each hourly pair), while I'_0 is shown by the dashed curves (rightmost bars in each hourly pair). Near local noon, OTD variability is driven by nonuniformity in pixel response, while LIS variability is driven by $P_{\alpha\tau}(I_B)$; the LIS sensor includes a very high threshold setting for bright (quasi-specular reflection) backgrounds that tend to occur near noon at low α (i.e., low θ) and, hence, reverses the general condition of minimum-detectable radiance decreasing toward the array corners. In general,

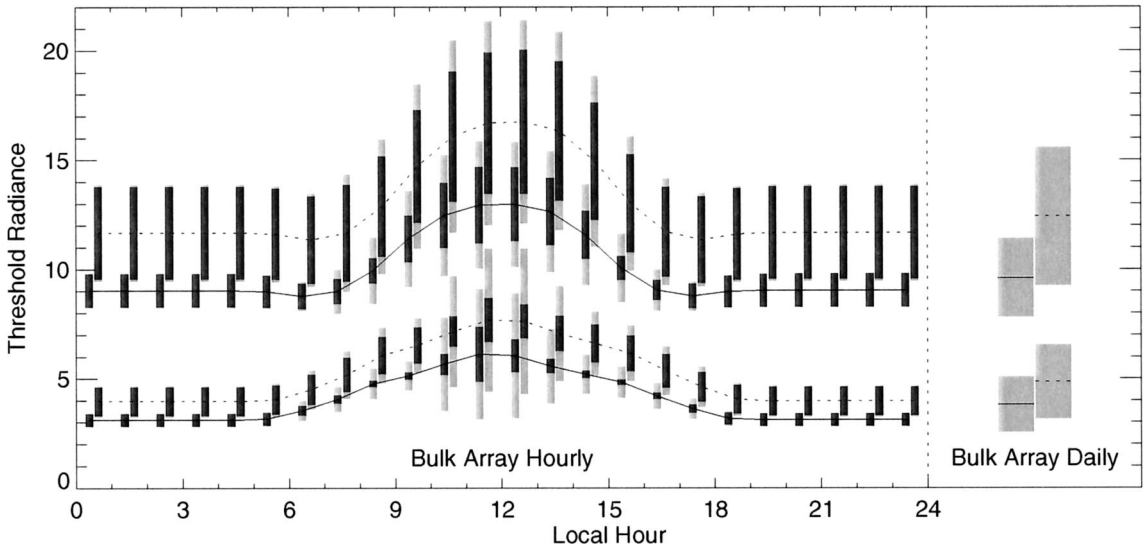

FIG. 5. FOV-weighted mean array applied threshold radiances (in μJ sr^{-1} m^{-2}), for OTD (upper pair of curves) and LIS (lower pair of curves). Solid curves and left bars in each hourly pair correspond to radiances incident on the instrument lens system I_0; dashed curves and right bars correspond to radiances emitted normal to cloud top I'_0. Light bars show σ_{I_0}, scatter due to variability in both background radiance and pixel response, while dark bars show $\sigma_{\overline{I}_0}$, scatter due to variability in pixel response alone. Daily means are shown at far right, and are weighted by $n_e(\tau)$, the number of actual events recorded at each local hour.

LIS minimum-detectable radiances are less variable than OTD.

c. Intrinsic SNR and FAR

Having determined $P_{\alpha\tau}(I_0)$, the diurnal cycle of OTD and LIS signal-to-noise ratio and false alarm rate due to intrinsic sensor noise may be computed, that is, SNR and FAR in a system comprising the instrument, lightning transients, and a stationary background scene without specular reflection or other external noise sources. The methodology employed here follows Christian et al. (1989), using parameters listed in Table 1. Treatment of the area A_s of the lightning source is modified. Christian et al. (1989) prescribed a fixed 10 km $\times$ 10 km lightning source, matching the assumed pixel size. Here, we estimate the typical area of lightning strokes (sensor pixel event ''groups'' within the same frame) as $\overline{n}_{eg}A_0$, the mean number of pixel events per stroke (7.8) observed by LIS near boresight, at night, and in the most sensitive quadrant, multiplied by the area of a LIS near-boresight pixel. This yields $\overline{A}_s = 98$ km^2, very close to the prior estimate. However, for SNR computation, A_s should in principle be prescribed as the smaller of actual pixel area $A(\mathbf{x})$ and $\overline{A}_s$. For all LIS pixels, and most OTD pixels at low to moderate θ, this effectively sets $A_s = A(\mathbf{x})$. For the FAR computation, $A(\mathbf{x})$ itself is always used. Also, it is appropriate to use I_0, the minimum detectable radiance incident upon the lens, for these calculations. Finally, the optical transmission has been estimated as 0.5 (H. J. Christian 2001, personal communication), but from $R'(\theta)$ it is apparent that this varies across the FOV. The estimated value is thus scaled accordingly.

TABLE 1. Values used in estimation of OTD and LIS SNR and FAR, using methodology detailed by Christian et al. 1989. (''C01'' denotes H. J. Christian 2001, personal communication).

Parameter	Definition	Value	Units	Reference
a	Lens aperture diameter	0.0033	m	C01
r	Sensor altitude	7.5, 3.5 $\times$ 10^5	m	Actual ephemeris
q	Pixel quantum efficiency	0.55	—	C01
k	Optical transmission	0.5 $R'(\theta)$	—	C01, this study
λ	Filter center	7.77 $\times$ 10^{-7}	m	Koshak et al. (2000a)
$\Delta\lambda$	Filter width	8.56, 9.09 $\times$ 10^{-10}	m	Koshak et al. (2000a)
τ	Frame integration time	0.0019	s	C01
n_r	The rms readout noise	100	—	C01
I_b	Background radiance	$I_B(\alpha,\tau)$	W m^{-2} sr^{-1} μm^{-1}	This study
I_s	Threshold energy density	$I_0(\mathbf{x},\tau \mid I_B)$	J m^{-2} sr^{-1}	This study
A_s	Source area	min (A (**x**), 9.8 $\times$ 10^7)	m^2	This study
A_p	Pixel area	A (**x**)	m^2	This study
α'	Cloud albedo	0.8	—	—

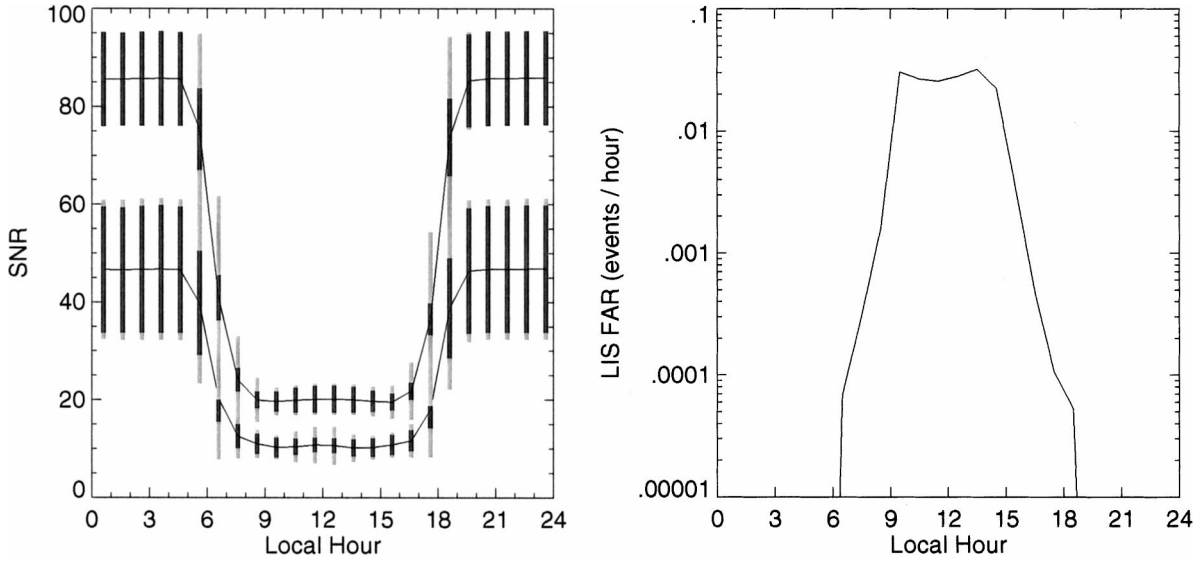

FIG. 6. (a) Computed SNR for (upper curve) OTD and (lower curve) LIS sensors. Threshold radiance I_0 is used. The σ bars are as in Fig. 5. (b) Computed FAR for the LIS sensor.

Shown in Fig. 6a are $\overline{\mathrm{SNR}}(\tau)$ and $\overline{\mathrm{SNR}}$ for OTD and LIS, with σ as in Fig. 5. Minimum SNR values (10 ± 2) are found in LIS during daytime but are well above the intrinsic SNR ~ 6 criterion cited by Christian et al. (1989) as acceptable levels. A single array FAR(τ) is computed as the sum of individual pixel FAR($\mathbf{x}$, τ), and is shown in Fig. 6b. For OTD, the intrinsic FAR is negligible (less than 10^{-34} s^{-1}); for LIS, FAR is small during daytime ($\sim 10^{-5}$ s^{-1}), and is expected to yield five false triggers per month. It is emphasized that this is only the FAR due to instrument noise; false event triggers from energetic particles impacting the array, or from quasi-specular reflection are not included in this computation; these are treated below.

d. External noise rejection

It was demonstrated above that internal sensor noise for the sensors is negligible. Instead, the CCD-based instruments are limited by external noise sources, including ambient radiation noise, solar ''glint'' (quasi-specular transient reflection from ocean surface or cloud tops), and cloud edge ''contrast'' artifacts (false transients due to a rapid change in background scene radiance as a pixel FOV crosses from dark land or ocean surface to a bright cloud). A series of software filters in the OTD/LIS data production code removes these noise sources.

Radiation impacting the CCD array at oblique angles generates single-frame streaks with much higher regularity and much larger scale than pixel triggers from true lightning. Radiation impacting the array at acute angles generates single-pixel, single-frame events that are usually discernible by their ''randomness,'' that is, there is little to no spatiotemporal persistence in either pixel or geographic coordinates. An exception is the South Atlantic anomaly (SAA; Pinto et al. 1992), a stationary feature of the earth's magnetic field whose centroid is currently near Sao Paulo, Brazil. Radiation noise rates within the SAA (and to a lesser extent, in high-latitude, near-polar regions) can be much higher; the production software filters are adaptively made more aggressive in these regions (the filters require greater spatiotemporal persistence for observed events to be retained as true lightning).

Optical artifacts from solar glint are characterized by long, persistent streams of very high radiance pixel events, and can only occur in regions observed at a very low glint angle γ, Fig. 2b. Typical lightning flashes contain roughly lognormal event radiance distributions; glint features are depleted in low-radiance events. Since quasi-specular reflection can occur from bright (and perhaps ''hard'') convective cloud tops, there is some natural covariance of rejected glint events with the actual deep convective cloud (and hence lightning) spatial distributions.

Optical artifacts from cloud edge contrast effects are partially a result of the specific OTD and LIS electronics design. They are characterized by intermittent streams of very low radiance pixel events typically no more than a pixel wide when examined in pixel coordinates. Again, since these require bright clouds to occur, there will be some covariance of the rejected contrast event spatial distribution with the actual lightning spatial distribution. As with glint, contrast noise only occurs during daytime.

Mixed in with the external noise are a subpopulation of lightning flashes, occurring during very low flash rate storms, which truly emit only a small number of pulses detectable by the sensors. Objectively, such flashes are inseparable from, for example, radiation noise; there is

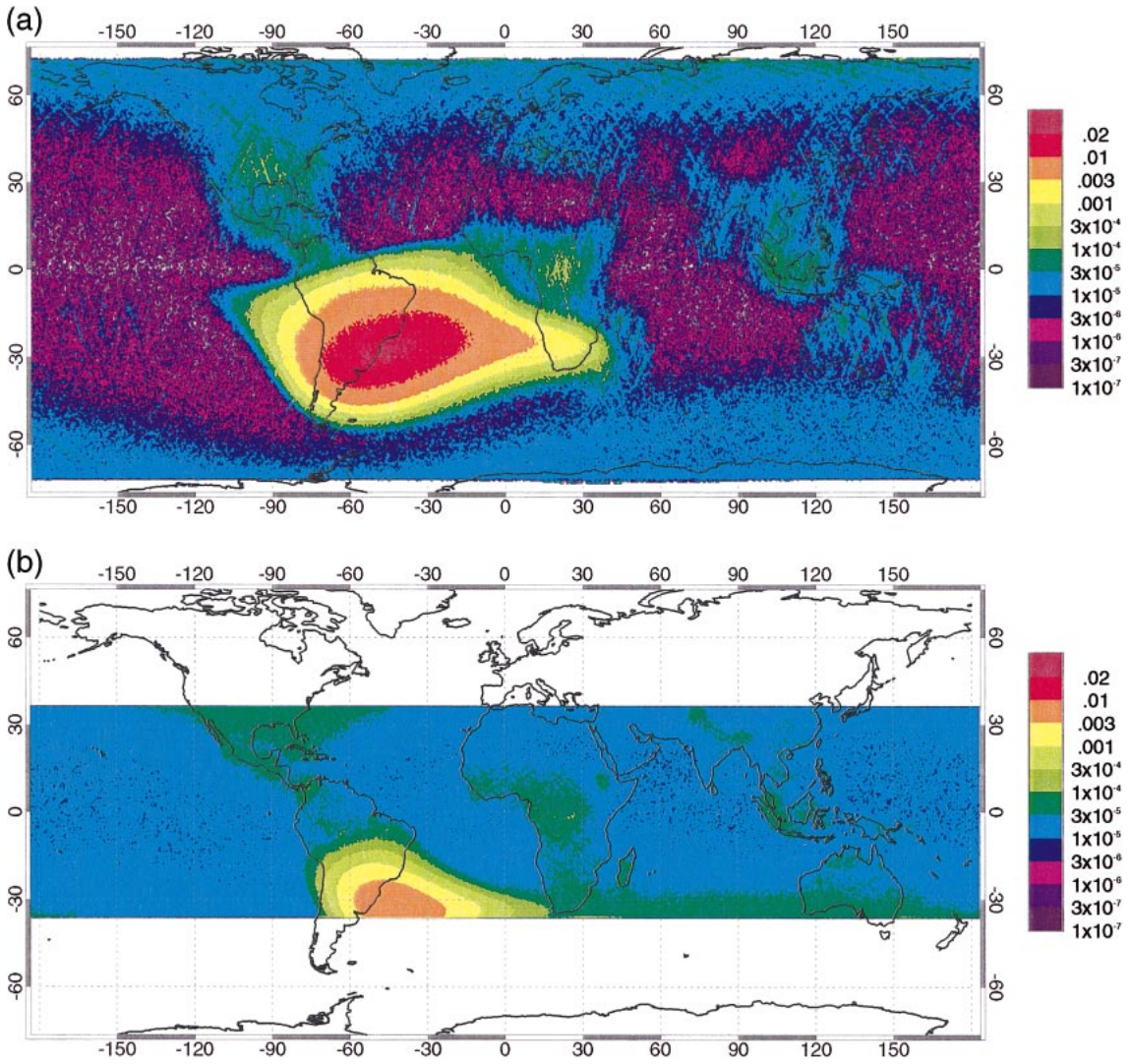

FIG. 7. Nighttime pixel event rejection rates by the (a) OTD and (b) LIS production code noise filters, in units of events per second per pixel.

simply too little observed information content to make a valid categorization. As such, both the OTD and LIS data are overfiltered; that is, there is an accepted population of flashes that are rejected from the final datastream, corresponding to a slight decrease in the flash detection efficiency predicted from OPS-based modeling. In the OTD dataset, ''borderline'' events and flashes were included in distributed data but tagged with a quality metric (the density index or thunderstorm area count). A baseline value of 140 was recommended for event acceptance; this threshold is employed here. In the LIS dataset, borderline events and flashes were removed during the production code stage, and are not included in the distributed (version 4) data. Since the rate of external noise rejection is nontrivial, and represents additional impacts beyond the present modeling, we here report the basic rates and distribution of actual noise rejection.

Figures 7a,b show the total nighttime pixel event rejection rates for OTD and LIS, respectively, for their complete missions to date. Since much noise is rejected prior to geolocation, noise rejection rates are recorded in the distributed data as a function of time alone (in 1-s intervals), hence array-total rejection rates are accumulated here at their nadir points for each second of the missions. This corresponds to a spatial uncertainty comparable to the instrument FOV area, that is, 1300 km $\times$ 1300 km and 650 km $\times$ 650 km for OTD and LIS, respectively. Since these are for nighttime (1800–0600 LST) conditions only, the rejected events are primarily composed of radiation noise and the subpopulation of ''low information content'' true flashes that are also rejected. The dominant feature is clearly the SAA, which is approximately twice as large for OTD (which orbits at a higher altitude). The composited results, of course, mask the fact that even SAA radiation noise is

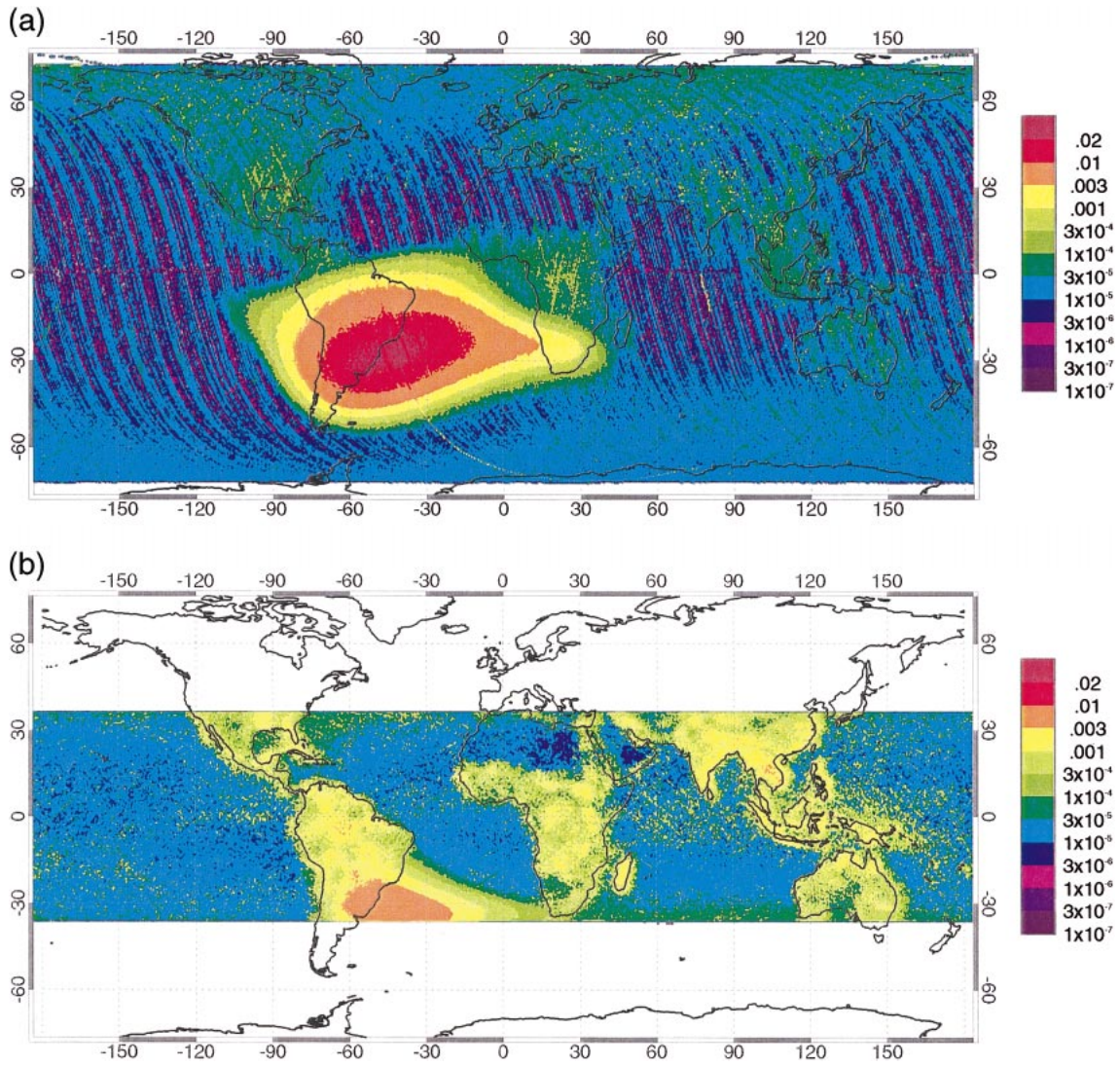

FIG. 8. Daytime pixel event rejection rates by the (a) OTD and (b) LIS production code noise filters, in units of events per second per pixel.

spatiotemporally random, and hence amenable to objective filtering. Radiation noise in polar regions is also evident and loosely follows contours of geomagnetic latitude. The DC noise rejection rate for LIS (i.e., the average value in lightning-free regions away from the SAA) can be estimated from lightning-free oceanic regions, and is approximately 10^{-5} events per second for each pixel or 0.2 events per second from the entire array. Clearly this is much higher than the intrinsic FAR computed above, and the sensor is limited by ambient, rather than instrument, noise. The DC rate for an OTD pixel is lower (10^{-6} events per second) presumably due to the OTD's higher pixel energy trigger thresholds.

Figures 8a,b show the total daytime pixel event rejection rates. Due to its increased resolution and higher sensitivity, the LIS records significantly more noise events from fixed-scale optical artifacts than the OTD; this is the primary reason for the discrepancy between the two plots. The increased LIS spatial covariance with the actual lightning distribution indicates either a higher false rejection rate of true flashes, or a true tendency of quasi-specular reflection to occur more frequently from ''hard-topped'' deep convection, presumably more common over land. The consistency between predicted flash detection efficiency (in the absence of external noise) and ground-validated flash detection efficiency (see below) argues for the latter interpretation, although an emphasis on daytime conditions in future ground validation studies is clearly warranted.

Table 2 shows the ratio of accepted to rejected pixel events for OTD and LIS, daytime and nighttime conditions, for some representative global regions. These can be considered the ''nominal'' instrument SNR (at the pixel event level) in the version 1.1 and version 4.0

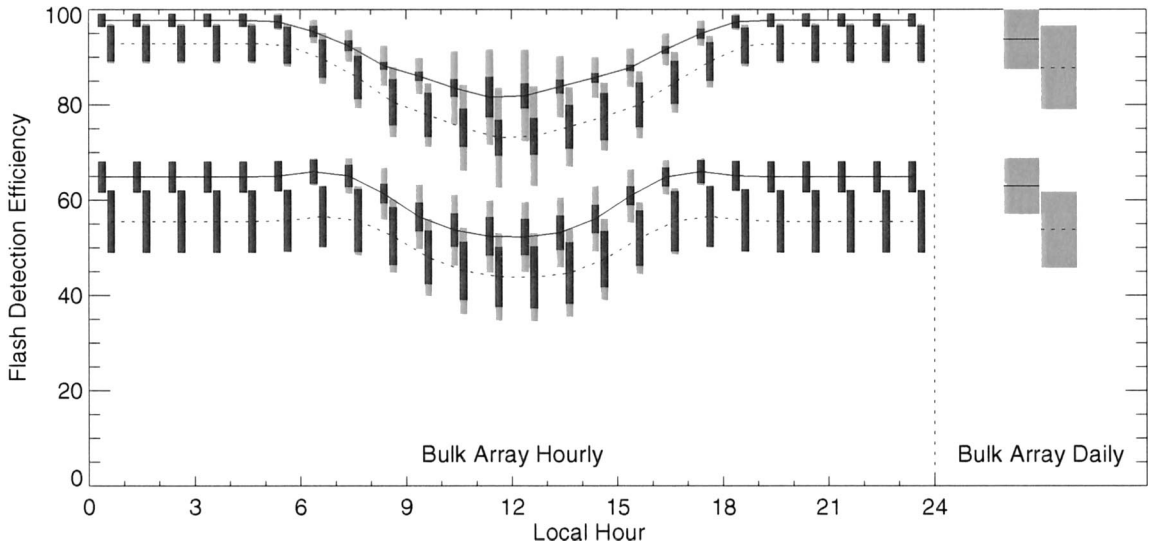

FIG. 9. Predicted flash detection efficiency F for (upper pair) LIS and (lower pair) OTD. Solid (I_0) and dashed (I_0') curves and error bar definitions are as in Fig. 5. Dashed curves are likely more consistent with the OPS truth dataset, but may still represent overestimates.

distributed OTD and LIS data. While not representative for the data product of primary interest (pixel event clusters, or ''flashes''), the nominal SNR does illustrate a 3–80-fold reduction during daytime conditions for LIS (1–3-fold reduction for OTD), and shows that in many locations, especially during daytime, at least as much LIS raw pixel data are discarded (albeit for objectively defensible reasons) as are retained.

e. Flash detection efficiency

Flash detection efficiency F (in the absence of external noise) is estimated here[7] (Fig. 9) by mapping the computed distribution $P_{\alpha\tau}(I_0)$ through the OPS truth curve, $F(I_0)$, the cumulative density function of OPS-observed flashes with observed peak pulse radiances $I^*_{\mathrm{OPS}} > I_0$ [see, e.g., Koshak et al. (2000a)]. As discussed above, caveats on the applicability of this truth curve due to nonuniformity in OPS pixel sizes, and OPS undersampling, apply. For at least some LIS and OTD pixels, the mean OPS pixel footprint A_{OPS} is smaller than that of LIS or OTD pixels A_1, so the bulk array results likely represent overestimates of flash detection efficiency (or equivalently, upper bounds).

It is emphasized that the error bars σ_F only represent uncertainty introduced by not controlling for instantaneous I_B or pixel response, and do not include any variance in the estimate of $F(I_0)$ itself, either from undersampling in the OPS dataset, or nonrepresentativeness of the OPS-observed storms for all local times and geographic locations. They are thus minimum estimates of σ_F. Nonetheless, they may now be used as one of the key inputs to variance estimates for OTD- or LIS-derived climatologies, or for individual storm cell flash rate estimates.[8]

4. Consistency of predicted diurnal cycles

Table 3 summarizes prior cross-sensor validation of the OTD and LIS sensor F, along with the appropriate predicted F from this study. Boccippio et al. (2000b) compared a large sample of National Lightning Detection Network (NLDN) truth flashes with OTD observations, and predicted the weighted diurnal mean OTD F for 8-bit threshold 15 (7-bit threshold 8, the same used in this study) to be 55%–70%. However, uncertainty in OTD's host platform attitude and ephemeris, and uncertainty in appropriate nominal flash times between the two sensors, forced a range of acceptable space–time differences to be allowed, and these may have been too tolerant, thus overestimating OTD F. Thomas et al. (2000) compared LIS and VHF/time-of-arrival (TOA) lightning mapping array (LMA) observations for a single overpass, and estimated LIS F to be 84%. While this is a small sample, the storms studied are likely similar in nature to storms in the OPS truth

[7] In this and subsequent papers, the convention will be established to refer to instrument flash detection efficiency as F, stroke (group) detection efficiency as G, and pixel (event) detection efficiency as ε. As with flashes, G can be defined as the percentage of all ''strokes'' (adjacent channel segment illuminations, discretized into 2-ms sampling frames) detectable by the sensors, and ε can be defined as the percentage of all radiant emitters, discretized into 2-ms sampling frames and fixed-sized integrating areas, detectable by the sensors.

[8] The other key input is the natural variance $\sigma^2_{f_c}$ in instantaneous flash rates themselves, which may be estimated from ground observations or bootstrapped from the complete LIS dataset. An important feature of the LIS-derived $P(f_c)$, as reported in (Boccippio et al. 2000a), is that the shape of this distribution is very similar over both land and ocean. This suggests that geographic variability in the intrinsic variance $\sigma^2_{f_c}$ is small, and a single value might be reasonably prescribed.

TABLE 2. ''Nominal'' pixel event SNR for the distributed OTD and LIS datasets (ratio of the number of pixel events retained as lightning components to the number rejected as noise contamination by the production software).

Region	Lat, Lon	LIS, night	LIS, day	OTD, night	OTD, day
Congo basin	0°, 20°E	32	0.83	4.1	3.4
Southeast Asia	15°N, 105°E	20	0.24	4.0	2.1
Amazon basin*	3°S, 63°W	19	0.36	0.12	0.19
North Australia	15°S, 135°E	14	0.34	4.1	2.0
Southeast United States	32°N, 90°W	12	0.65	3.8	3.3
Gulf Stream	32°N, 75°W	11	3.3	3.4	3.2
GATE domain	12°N, 18°W	11	0.25	2.1	1.4
TRMM/LBA domain*	10°S, 63°W	8.2	0.44	0.037	0.069
Mediterranean	32°N, 20°E	5.0	0.92	2.8	1.6
SPCZ	15°S, 150°E	5.0	0.84	2.7	0.97
South Africa*	30°S, 20°E	3.6	0.75	0.052	0.078
COARE domain	0°, 160°E	0.71	0.038	2.7	0.41
South Brazil*	30°S, 60°E	0.57	0.19	0.012	0.0094

* Regions within the South Atlantic anomaly.

dataset. The LMA is a very high sensitivity network, hence the OPS LIS F does appear to be an overestimate for nighttime conditions. Similarly, Ushio et al. (1999) examined a small sample of flashes during an overpass of the Kennedy Space Center (KSC) VHF/TOA Lightning Detection and Ranging (LDAR) and NLDN networks, and found F to be 57%. Koshak et al. (2000b) examined overpasses of the LDAR and KSC electric field mill (EFM) network during evening and nighttime, and found $F \sim 92\%$. This study was more carefully controlled than the preliminary investigation of Ushio et al. (1999) in that it screened out truth flashes that could not confidently be determined to have occurred within the LIS FOV, or outside periods of documented sensor data buffer overflow.[9] Both results support the contention that OPS-based F is an overestimate.

Alternatively, the relative behavior of OPS-based F appears consistent with the prior studies. Boccippio et al. (2000b) found a ±2%–7% difference in day and night OTD F, consistent with the ±6% predicted here. Similarly, Boccippio et al. (2000a) found that the ratio of LIS and OTD F, as derived from climatological bulk flash rate density estimates in 2.5° × 2.5° grid cells, was 1.65:1, nearly identical to the 1.67:1 ratio predicted by OPS. Since the most likely source of error in the OPS-based estimates (neglect of pixel footprint A) should have similar variability in its relative day/night and OTD/LIS impacts on F, the consistency of the observed and predicted relative response supports the idea that OPS-based estimates reasonably reflect variability in the instruments' response, but are high biased due to ''underfilling'' of some actual OTD and LIS pixel footprints by OPS truth pixel observations. If true, then the σ_F reported here may reasonably be used as minimum estimates in variance decompositions of OTD or LIS climatologies and storm flash rate estimates.

[9] Without this correct screening, the estimated F would have been 78%, demonstrating the need for extreme care in determining cross-sensor (x, y, t) FOV overlaps during validation.

5. Conclusions

The diurnal variability in OTD and LIS performance has been estimated, driven by estimates of the distribution of observed background radiances $P_{\alpha\tau}(I_B)$, and constrained by laboratory calibration estimates of relative instrument response across their FOV. Here I_B is a ''driver'' in that it determines instrument threshold, both through selecting prescribed values and altering the instrument amplifier response. Five primary sources of variability are important.

1) Variability in the instrument DC amplifier gain G between sensor pixel quadrants, implicit in the laboratory calibrations.

TABLE 3. Prior cross-sensor estimates of OTD and LIS flash detection efficiency F, with corresponding predictions from this study (last column). In Boccippio et al. (2000a,b), flashes were defined (i.e., clustered from optical pulses) using the operational v 1.1 and 4.0 data production algorithms for OTD and LIS, respectively. In Thomas et al. (2000), Ushio et al. (1999), and Koshak et al. (2000b), flashes were manually identified by examination of substructure data (optical pulses, VHF sources, electric field waveforms, etc.).

Study	Sensors	τ	Flashes	F Result	F Prediction
Boccippio et al. 2000b	OTD/NLDN	All	4571	≤55%–70%	≤46%–62%
Thomas et al. 2000	LIS/LMA/NLDN	0116	128	84%	≤93%–97%
Ushio et al. 1999	LIS/LDAR/NLDN	1740	122	≥57%	≤83%–94%
Koshak et al. 2000	LIS/LDAR/EFM/NLDN	1800–0500	77	92%	≤87%–97%
Boccippio et al. 2000b	OTD/NLDN	All	4571	±2%–7% day/night	±6% day/night
Boccippio et al. 2000a	LIS/OTD	All	3×10^6	LIS = 1.65 × OTD	LIS = 1.67 × OTD

2) Variability in the combined lens/filter response with off-boresight angle θ, that is, $R'(\theta)$. OTD and LIS corner pixels receive 16%–18% less of the same incident I that would be passed at boresight, and this effect is not represented in the AC calibration lookup tables. This correction thus should be applied to normalize the population of radiances incident upon the lens.
3) Variability in the actual background radiance I_B, which also has some covariance with the cloud-sensor angle α (itself correlated to θ) near local noon.
4) Variability in the amount of lightning pulse radiance emitted normal to cloud top and at the cloud-sensor angle α (due to scattering within clouds), important for comparisons with ''truthing'' datasets sampled at fixed α.
5) Variability in the pixel footprint A, again important for comparisons with truthing datasets collected with different or variable A.

Of these, items 1–4 have been controlled in this study.

From this, it is found that bulk (pixel FOV weighted) applied radiance thresholds, expressed as lightning pulse radiances emitted normal to cloud top, are 11.7 ± 2.2 and 16.8 ± 4.6 μJ sr^{-1} m^2 for OTD night and local noon (at sensor threshold 15), and 4.0 ± 0.7 and 7.6 ± 3.3 μJ sr^{-1} m^2 for LIS night and local noon. Minimum intrinsic instrument signal-to-noise ratio occurs between 0800 and 1600 local time, and is 20 ± 3 and 10 ± 2 for OTD and LIS, respectively. The false alarm rate due to intrinsic sensor noise is effectively zero for OTD, and low for LIS (~5 false triggers per month). The false alarm rate due to high-energy ambient radiation is significantly higher (for LIS, 0.2 s^{-1}, outside of the South Atlantic anomaly; for OTD, 0.02 s^{-1}). Filtering of optical artifacts during daytime scenes yields an event rejection rate up to 100 times higher than the radiation event rejection rate.

Hourly and daily instrument bulk flash detection efficiency F is predicted by mapping the distribution of applied radiance thresholds through a ''truth'' relation from the U2 optical pulse sensor, $F(I_0)$. Allowing for in-cloud scattering and reduction of emitted lightning radiance at α, this predicts 93 ± 4% and 73 ± 11% LIS F at night and local noon, and 56 ± 7% and 44 ± 9% OTD F at night and local noon. Equivalently, a single bulk daily F estimate (not considering diurnal variability) would be 88 ± 9% and 54 ± 8% for LIS and OTD, respectively. These are likely overestimates (upper bounds) of F, based on the expected effects due to not controlling the pixel footprint A and supported by cross-sensor validation studies. These studies do suggest that the *relative* behavior of OPS-based predictions is consistent with observation, and thus that the σ_F estimates may reasonably be used as lower bounds in variance decompositions of OTD and LIS climatologies or individual storm flash rate estimates.

Variability in pixel footprint A, and subpixel filling of emitted pulses, is likely an important factor in refining these estimates. This finding stresses the importance of either controlling for A (and α) in future OPS measurements, or of reporting it. Alternatively, observations from the smallest and most sensitive LIS pixels (those near boresight, in the most sensitive quadrant, at night), may be used as a bootstrap truthing dataset with controlled A with which to assess relative instrument performance off boresight and during daytime. This bootstrap analysis is explored in the second paper in this series.

Acknowledgments. This research was supported by Grant NRA-97-MTPE-03, under the direction of Dr. David O'C. Starr. Thanks are given to Hugh Christian and Mike Stewart for helpful discussions and commentary.

APPENDIX

Bootstrapping a Controlled-Sampling Truth Dataset

LIS boresight pixels under the most sensitive viewing conditions (night) offer a bootstrapped ''truthing'' dataset against which off boresight and daytime performance may be assessed. They have the further advantage of having a controlled viewing geometry, unlike the OPS dataset. However, the pixel trigger conditions for off-boresight observations must first be expressed in terms of observations sampled under the boresight viewing geometry.

LIS corner pixel footprints are approximately 4 times larger than LIS boresight footprints, and OTD corner pixel footprints are approximately 13 times larger than LIS boresight footprints. The LIS off-boresight trigger condition may be written:

$$\sum_{i=1}^{N} \frac{I_i^*(\mathbf{x}_0)\,\cos\alpha_1}{R(\theta_0)} \frac{A_0}{A_1} > I_0(\mathbf{x}_1), \tag{A1}$$

where the LIS-boresight pixel event radiance population taken within observed strokes $P(I^*)$ is sampled N events at a time, with N given by the number of boresight pixel footprints required to fill an off-boresight pixel footprint, that is, the closest integer to A_1/A_0. The covariance between emitter radiances within individual strokes necessitates this sampling strategy. Recalling Eq. (5), the trigger condition within an LIS quadrant, relative to boresight threshold radiance $I_0(\mathbf{x}_0)$, and defining boresight lens response as unity, would be

$$\sum_{i=1}^{N} I_i^*(\mathbf{x}_0) > I_0(\mathbf{x}_0) \frac{1}{R'(\theta_1)\,\cos\alpha_1} \frac{A_1}{A_0}, \tag{A2}$$

with I^* sampled from near-boresight observations as above. Thus for LIS corner pixels to trigger, the sum of 4 concurrent LIS-boresight footprint-sized emitters (normal to cloud top) would have to exceed roughly 8 $I_{0,\mathrm{LIS}}(\mathbf{x}_0)$. Given the OTD boresight threshold [roughly 3 $I_{0,\mathrm{LIS}}(\mathbf{x}_0)$], the sum of 5 equivalent emitters would have

to exceed 15 $I_{0,\mathrm{LIS}}(\mathbf{x}_0)$ at OTD boresight, and the sum of 13 equivalent emitters would have to exceed 94 $I_{0,\mathrm{LIS}}(\mathbf{x}_0)$ at the OTD corner. Equivalently, the emitters in these pixels would need to emit an average radiance (normal to cloud top) of $2\times$, $3\times$ and $7\times$ $I_{0,\mathrm{LIS}}$ and be completely pixel filling.

The use of LIS boresight pixels to bootstrap a relative detection efficiency estimate is treated in the second paper in this series.

REFERENCES

Boccippio, D. J., S. J. Goodman, and S. Heckman, 2000a: Regional differences in tropical lightning distributions. *J. Appl. Meteor.*, **39,** 2231–2248.

——, and Coauthors, 2000b: The Optical Transient Detector (OTD): Instrument characteristics and cross-sensor validation. *J. Atmos. Oceanic Technol.*, **17,** 441–458.

Christian, H. J., and S. J. Goodman, 1987: Optical observations of lightning from a highaltitude airplane. *J. Atmos. Oceanic Technol.*, **4,** 701–711.

——, R. J. Blakeslee, and S. J. Goodman, 1989: The detection of lightning from geostationary orbit. *J. Geophys. Res.*, **94,** 13 329–13 337.

——, ——, and ——, 1992: Lightning imaging sensor for the Earth Observing System. NASA TM-4350, 44 pp.

——, K. T. Driscoll, S. J. Goodman, R. J. Blakeslee, D. A. Mach, and D. E. Buechler, 1996: The Optical Transient Detector (OTD). *Proc. 10th Int. Conf. on Atmospheric Electricity,* Osaka, Japan, ICAE, 368–371.

——, and Coauthors, 1999: The Lightning Imaging Sensor. *Proc. 11th Int. Conf. on Atmospheric Electricity,* Guntersville, AL, NASA, 746–749.

Goodman, S. J., H. J. Christian, and W. D. Rust, 1988: A comparison of the optical pulse characteristics of intracloud and cloud-to-ground lightning as observed above clouds. *J. Appl. Meteor.*, **27,** 1369–1381.

Koshak, W. J., J. W. Bergstrom, M. F. Stewart, H. J. Christian, J. M. Hall, and R. J. Solakiewicz, 2000a: Laboratory calibration of the Optical Transient Detector and Lightning Imaging Sensor. *J. Atmos. Oceanic Technol.*, **17,** 905–915.

——, E. P. Krider, and D. J. Boccippio, 2000b: LIS validation at the KSC-ER. *EOS, Trans. Amer. Geophys. Union,* **81** (48), F47.

Pinto, O., W. Gonzalez, R. Pinto, A. Gonzalez, and O. Mendes, 1992: The South Atlantic Magnetic Anomaly: Three decades of research. *J. Atmos. Terr. Phys.*, **54,** 1129–1134.

Thomas, R. J., P. R. Krehbiel, W. Rison, T. Hamlin, D. J. Boccippio, S. J. Goodman, and H. J. Christian, 2000: Comparison of ground-based 3-dimensional lightning mapping observations with satellite-based LIS observations in Oklahoma. *Geophys. Res. Lett.*, **27,** 1703–1706.

Thomason, L. W., and E. P. Krider, 1982: The effects of clouds on the light produced by lightning. *J. Atmos. Sci.*, **39,** 2051–2065.

Ushio, T., K. T. Driscoll, S. Heckman, D. J. Boccippio, W. J. Koshak, and H. J. Christian, 1999: Initial comparison of the Lightning Imaging Sensor (LIS) with Lightning Detection and Ranging (LDAR). *Proc. 11th Int. Conf. on Atmospheric Electricity*, Guntersville, AL, NASA, 738–741.